Earth, Planets and Space
a SpringerOpen Journal

LETTER   Open Access

Effect of stress state on slow rupture propagation in synthetic fault gouges

Ken-ichi Hirauchi[1*] and Jun Muto[2]

Abstract

Slow slip events (SSEs) in subduction zones are known to proceed so sluggishly that the associated slow ruptures do not generate any detectable radiating seismic waves. Moreover, they propagate at speeds at least four orders of magnitude slower than regular earthquakes. However, the underlying physics of slow slip generation has yet to be understood. Here, we carry out laboratory studies of unstable slip along simulated fault zones of lizardite/chrysotile (liz/ctl) and antigorite (i.e., low- and high-temperature serpentine phases, respectively) and olivine, under varying conditions of normal stress, with the aim of better understanding the influence of stress state on the process of slow rupture along the plate interface. During a single unstable slip, we clearly observe a slow rupture phase that is often followed by an unstable, high-speed rupture. We find that lower fault-zone friction coefficients (μ values from 0.7 down to 0.5) lead to increasing degree of the slow rupture mode, and also that the slow rupture velocities ($V_r = 0.07$ to 5.43 m/s) are largely consistent with those of short-term SSEs observed in nature. Our findings suggest that the generation of SSEs is facilitated by conditions of low normal stress and low fault-zone strength along the plate interface, which may be weakened by metamorphic reactions that result in the production of hydrous phases (e.g., serpentine) and/or the direct involvement of fluid itself, leading to a reduction in effective normal stress.

Keywords: Fault gouge; Rupture velocity; Serpentine; Slow slip; Subduction zone; Unstable slip

Findings

Introduction

In the last decade, a variety of unusual earthquakes have been observed in circum-Pacific subduction zones, including non-volcanic tremors, low-frequency earthquakes (LFEs), and slow slip events (SSEs) (e.g., Dragert et al. 2001; Obara 2002; Shelly et al. 2006; Peng and Gomberg 2010; Beroza and Ide 2011). All of these seismic phenomena appear to be related to shear slip along and/or near the plate interface and occur at the same time and place (e.g., Rogers and Dragert 2003; Ito et al. 2007). The co-existence of anomalously high Poisson's ratios (approximately 0.4) with the source regions for tremors and LFEs suggests that aqueous fluids in these areas, released from dehydration reactions in the subducting oceanic crust, are present under conditions of elevated pore pressure (Audet et al. 2009; Peacock et al. 2011). As a direct consequence, such elevated pore-fluid pressure acts to reduce the effective normal stress on the plate interface.

An individual SSE represents a transient release of strain that occurs in the transition zone between locked and stable sliding zones, characterized by low rupture velocity (approximately 1 to 10 km/day), long duration (days to years), and no measurable radiating seismic energy (e.g., Ide et al. 2007). In southwest Japan, short-term SSEs and tremors have been observed to occur preferentially along the plate interface directly beneath the hydrated mantle wedge (Kato et al. 2010). This is attributed to the regional development of a substantially weak shear zone (10^1 to 10^3 m thick) along this portion of the plate interface caused by the presence of hydrous minerals such as serpentines and talc (Hirauchi et al. 2010b; Kawano et al. 2011; Hirauchi et al. 2013). These geophysical observations seem to suggest that fluids play an important role in facilitating slow slip under low stress conditions (Shelly et al. 2006), although the physical mechanisms underlying the generation of SSEs are not yet fully understood (Rubinstein et al. 2004; Ben-David et al. 2010a).

* Correspondence: skhirau@ipc.shizuoka.ac.jp
[1]Department of Geosciences, Graduate School of Science, Shizuoka University, 836 Ohya, Suruga-ku, Shizuoka 422-8529, Japan
Full list of author information is available at the end of the article

The stick-slip (or unstable slip) frictional instability on preexisting faults is widely regarded as a possible mechanism for the generation of earthquakes. Recent numerical and experimental studies have shown that, depending on friction and stress conditions, slow rupture modes occur either as isolated events or in conjunction with much faster modes (Rubinstein et al. 2004; Ben-David et al. 2010a; Nielsen et al. 2010; Kaneko and Ampuero 2011; Bar Sinai et al. 2012). However, previous laboratory experiments on rocks have focused on stick-slip events for bare surfaces of granite and dunite under a relatively narrow range of normal stress conditions (equivalent to less than approximately 10 MPa) (e.g., Johnson and Scholz 1976; Okubo and Dieterich 1984; Kato et al. 1992; Ohnaka and Shen 1999), although the values of duration and propagation velocity for the SSEs (Gao et al. 2012) may be influenced by variations in effective normal stress on the plate interface. In the present study, we report observations of unstable slip events generated in synthetic fault zones, each of which represents a suitable analog for studying slow slip regions (Kato et al. 2010) through triaxial loading at confining pressures ranging from 60 to 170 MPa in order to explore how the properties of slow rupture change across a much wider range of physical conditions. All measurements were carried out under dry conditions, assuming that the fluids only act to reduce the effective confining pressure. Specifically, we investigate the effects of normal stress and frictional strength on the emergence of the slow rupture phase within various fault zone materials.
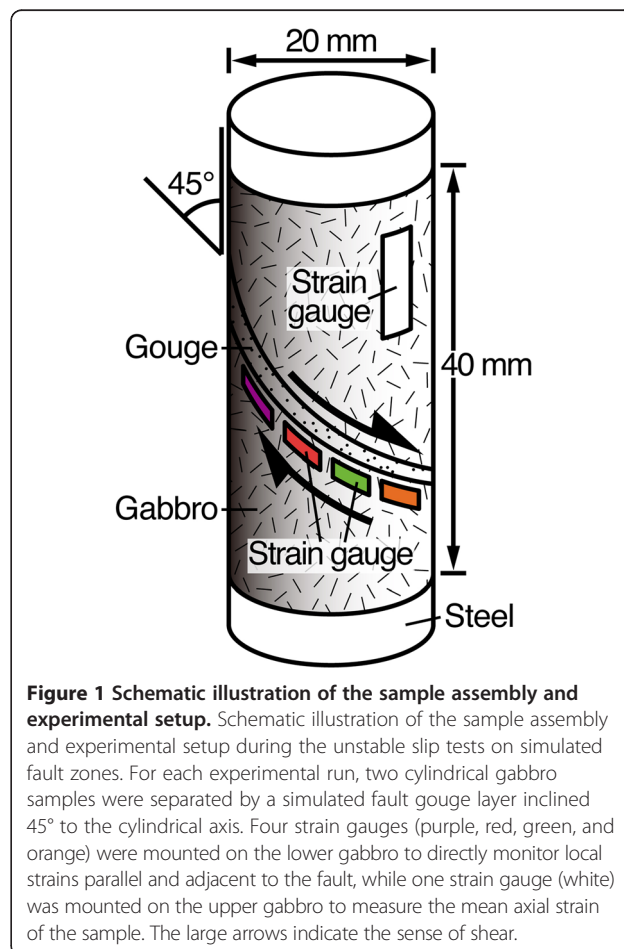
Experimental approach

Starting materials

The starting materials used for the low-T type (lizardite/chrysotile) and high-T type (antigorite) serpentines were natural serpentinites collected from the Mineoka ophiolite, central Japan, and from the Nagasaki metamorphic rocks, southwest Japan, respectively. These serpentinite samples are from the same stocks used by Hirauchi et al. (2010a) and Hirauchi and Katayama (2013) in their high-pressure deformation experiments. The rock samples used in the production of the low-T type serpentine mineral powders show mesh texture (Wicks and Whittaker, 1977), consisting of polyhedral, isotropic 'cores' (a mixture of chrysotile nanotubes and magnetite dust) enclosed by fibrous 'rims' (stacks of lizardite crystals) (Hirauchi et al. 2010a). The rock samples used in the production of the high-T type serpentine mineral powders exhibit interpenetrating textures (Wicks and Whittaker 1977), comprising 'almost randomly' oriented, platy, or acicular antigorite grains that range from 10 to 150 μm in length, as well as finely disseminated magnetite. The starting materials used in the production of the olivine mineral powders were prepared from a sample of San Carlos olivine (Fo$_{90}$). All

mineral powder samples in this study were pulverized, cleaned, sieved to <100 μm, then air dried at approximately 70°C for several days before being used in each experiment.

Experimental procedure

Unstable slip experiments were conducted in a gas-medium apparatus at room temperature (approximately 25°C), confining pressures (P_c) of 60, 100, 140, 160, and 170 MPa, and a nominal strain rate of 1×10^{-3} s^{-1}. Argon gas was used as the confining pressure medium. Cylindrical samples of gabbro, 20 mm in diameter and 40 mm in length, were cut in half along a plane oriented at an angle of 45° to the cylindrical axis (Figure 1). The pre-cut surfaces were first ground flat and then brought to a fine polish using a 3-μm diamond paste. For each experiment, 0.3 g of mineral powder was placed between the pre-cut, polished gabbro surfaces to produce a approximately 0.7-mm-thick layer of simulated fault gouge. Steel spacers were then placed at each end of the cylindrical sample assembly. In addition, a thin layer of Teflon was placed at the end of the piston to accommodate lateral slip of the sample assembly during deformation. The entire sample

Figure 1 Schematic illustration of the sample assembly and experimental setup. Schematic illustration of the sample assembly and experimental setup during the unstable slip tests on simulated fault zones. For each experimental run, two cylindrical gabbro samples were separated by a simulated fault gouge layer inclined 45° to the cylindrical axis. Four strain gauges (purple, red, green, and orange) were mounted on the lower gabbro to directly monitor local strains parallel and adjacent to the fault, while one strain gauge (white) was mounted on the upper gabbro to measure the mean axial strain of the sample. The large arrows indicate the sense of shear.

assembly was jacketed in a Teflon tube with 0.5-mm-thick walls, in order to isolate the sample from the confining medium.

Four strain gauges, each with an active gauge length of 1 mm, were mounted on the lower gabbro cylinder at 3-mm intervals along the saw-cut. The gauges were situated at a distance of 1 mm from the fault to directly monitor the fault-surface-parallel component of the strain field during each experiment (Figure 1). Note that the gauges at these four locations measure only one component of the strain tensor, parallel to the fault surface. Another strain gauge (with an active gauge length of 6 mm) was mounted to the upper gabbro cylinder, parallel to the cylindrical axis, in order to measure the axial strain of the sample (Figure 1). For each deformation experiment, the rupture velocity was calculated by measuring the time taken by the rupture to pass from one strain gauge to another (for the gauges situated adjacent to the saw-cut). It is important to note that since the rupture is most likely to propagate at an angle to the edge of the cylinder, the calculated velocity is an apparent velocity and is an upper bound for the rupture velocity.

At the start of each experimental run, the confining pressure was first raised to the desired value, after which an axial load was applied to the sample assembly at a loading velocity of 40 µm/s. Axial stress was determined by multiplying the axial strain by the Young's modulus of gabbro (E approximately 87.2 GPa). During these experiments, an increase in axial stress leads to a concomitant increase in both the shear stress and normal stress acting on the saw-cut. Note that the values of confining pressure investigated are equal to those of the initial normal stress before deformation.

All signals were amplified using signal conditioners (model CDV 700A, Kyowa Co., Ltd., Tokyo, Japan) with an input impedance of 10^7 Ω and a frequency limit of 500 kHz. The amplified signals were recorded on a computer at a sampling rate of 1 to 2 MHz for all seven channels, synchronously and continuously, using the Simultaneous-Sampling Multifunction DAQ NI-6110 and LabVIEW 2009 (National Instrument Co., Ltd., Austin, USA). Additional information on the details of data acquisition in this study can be found in Onuma et al. (2011).

Results

Mechanical data

Shear stress versus time (i.e., strain) curves for the samples deformed at P_c = 60 to 170 MPa initially exhibit a phase of linear elastic behavior, followed by a span of strain hardening, during which stress increases with strain and, finally, a third stage in which the stress levels off or drops until one sudden, large unstable slip occurs (Figure 2A). This type of sliding behavior is similar to that observed for dry gouge subjected to triaxial friction experiments at room temperature (e.g., Morrow et al., 1982). Furthermore, note that for low- and high-temperature serpentine gouges, the loading velocity of 40 µm/s carried out in this study lies in the velocity-weakening regime, where the slip potentially may be unstable (Reinen et al., 1994; Moore et al. 2004). The coefficient of friction, µ, which is defined as the ratio of shear stress to effective normal stress, was 0.48 to 0.58 for liz/ctl and 0.67 to 0.72 for antigorite (Figure 2B). This is in good agreement with the values reported from previous rock-on-rock friction experiments on liz/ctl and antigorite under similar conditions (Dengo and Logan, 1981; Reinen et al., 1994). This major difference in strength observed between liz/ctl and antigorite can be attributed to the corresponding differences in (001) bond strength for these two phyllosilicate varieties (e.g., Moore and Lockner, 2004). Olivine, on the other hand, yields a slightly higher and narrower range of µ values of 0.72 to 0.73 (Figure 2B).
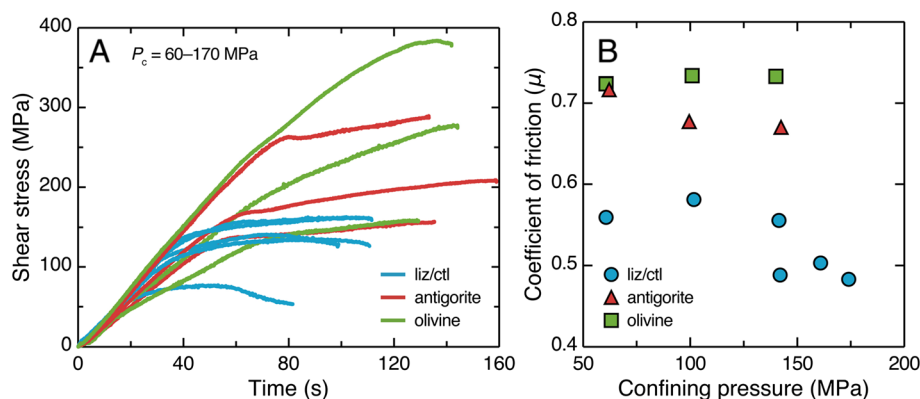

Figure 2 Shear stress versus time curves and plot of the coefficient of friction. (A) Shear stress versus time curves for each deformation experiment, leading up to a point just before the onset of unstable slip events. All experiments were run at a constant axial velocity of approximately 40 µm/s. **(B)** Plot of the coefficient of friction (µ) as a function of confining pressure (P_c). The values for the coefficient of friction displayed on this plot correspond to those recorded at the point in the experiments when maximum shear stress was achieved during shearing.

Unstable slip event

Figure 3 shows three representative experimental datasets, each comprising four plots of localized strain along the saw-cut versus time, and a single plot of mean shear stress versus time, throughout an unstable slip event. For most of the unstable slip experiments carried out in this study, a rupture event nucleated at one end of the fault in the shear direction and propagated to the other, as shown in Figure 3. In the experiments carried out at $P_c = 100$ and 140 MPa for antigorite and olivine, shear stress was observed to drop rapidly to a residual value during a brief period lasting only about 50 μs or less (Figures 3A,D and 4). In Figure 3D, it is also clear that the orange gauge placed at the lower edge of the saw-cut (Figure 1) first started to record compression just before the onset of this drop in shear stress, at which point the mode of deformation switches from a compressional to an extensional phase. This compression followed by extension is interpreted to reflect the propagation of the rupture along the simulated gouge layer (e.g., Johnson and Scholz 1976; Dieterich 1978; Okubo and Dieterich
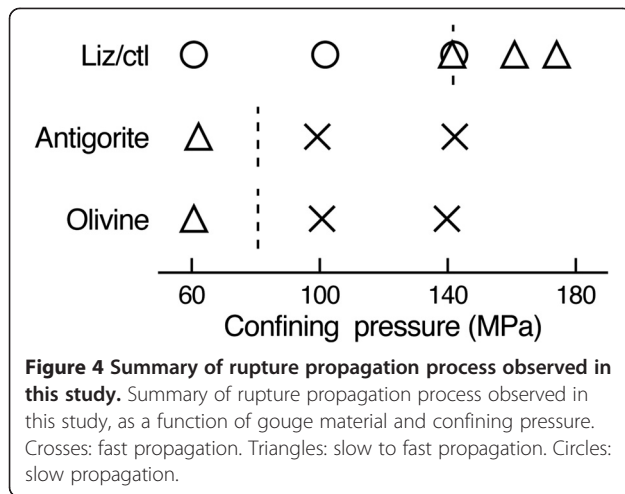
1984). Accordingly, we used this criterion to identify the peak compressional event recorded by each gauge as the rupture front propagated through each localized region (see arrows in Figure 3D-F), which then enabled us to calculate the apparent rupture velocity. Based on these calculations, the induced ruptures appear to have propagated laterally along the 45° angle simulated faults (gouges) at speeds of roughly a few kilometers per second. After the observed large stress drop, all strain gauges then recorded a series of large oscillations, which we interpret as possible resonances of the sample and loading machine due to the radiation of seismic energy.

In the experiments conducted at $P_c = 140$ to 170 MPa for liz/ctl and $P_c = 60$ MPa for antigorite and olivine, the shear stress was observed to initially decrease at a relatively slow rate during an approximately 10- to 385-ms time period, followed by a second, comparatively rapid drop in the space of approximately 50 μs or less (Figures 3B,E and 4). The plots of localized strain shown in Figure 3E indicate that rupture initiation took place at the lower edge of the saw-cut (orange gauge) and then propagated slowly
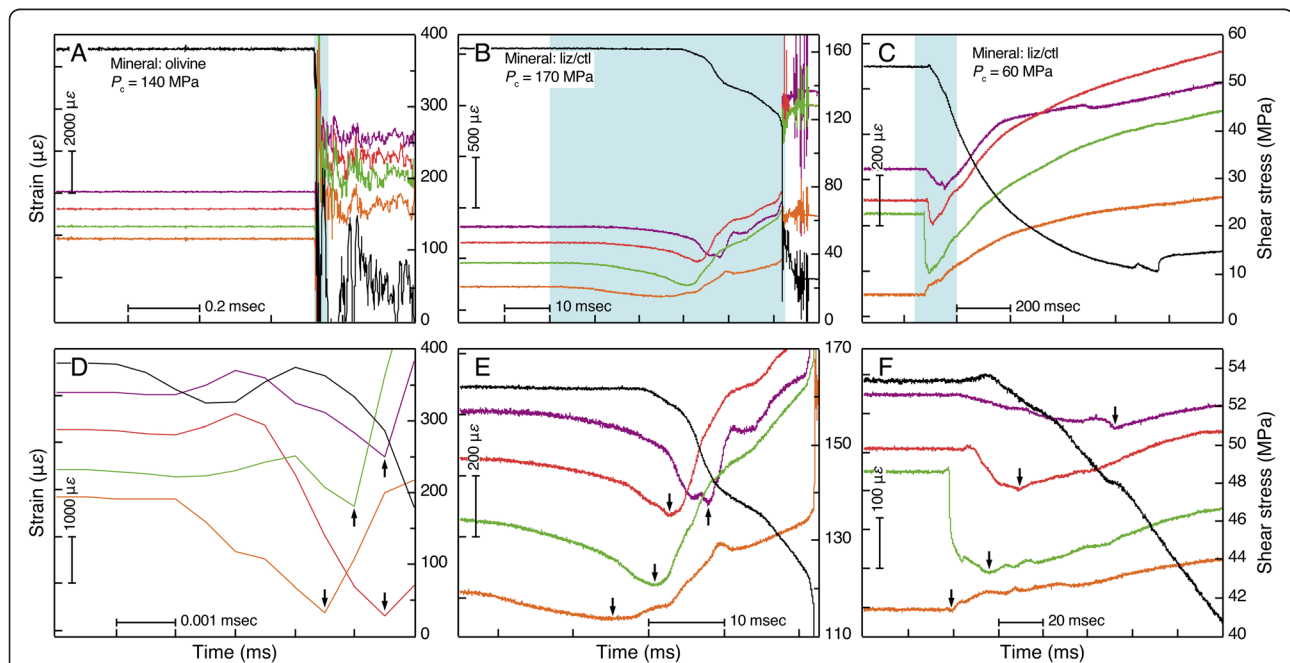
Figure 3 Three representative examples of experimental datasets. Three representative examples of experimental datasets showing, on the left axes, the evolution (with time) of local strains (purple, red, green, and orange) parallel to the fault, and, on the right axes, mean shear stress (black), during an unstable slip event. The strain versus time curves are offset vertically from each other for clarity. Note that the strain values reported correspond to the ε_{tt} component of the strain tensor, where t is the direction tangential to the fault, and that positive and negative strains correspond to extension and compression parallel to the pre-cut surface, respectively. The colors associated with local strains correspond to the colors assigned to the strain gauges shown in Figure 1. The blue regions shown in **A**, **B**, and **C** demarcate the locations on these plots that correspond to the close-ups shown in **D**, **E**, and **F**, respectively. The arrows in D to F indicate the time of peak compression recorded by each strain gauge, reflecting the passage of a rupture front through that region of the sample assembly. **(A and D)** Olivine gouge ($P_c = 140$ MPa). During this experimental run, the shear stress dropped within approximately 50 μs, with fast rupture propagation taking place at speeds of a few kilometers per second. **(B and E)** Liz/ctl gouge ($P_c = 170$ MPa). During this experimental run, a slow stress drop associated with multiple slow rupture propagation events persisted for approximately 20 ms, after which a fast drop in stress (as shown in **A** and **D**) occurred at seismic speeds. **(C and F)** Liz/ctl gouge ($P_c = 60$ MPa). During this run, a slow stress drop persisted for approximately 1 s until a residual stress level was achieved. Note that no high-frequency elastic radiation was observed after the unstable slip event.

Figure 4 Summary of rupture propagation process observed in this study. Summary of rupture propagation process observed in this study, as a function of gouge material and confining pressure. Crosses: fast propagation. Triangles: slow to fast propagation. Circles: slow propagation.
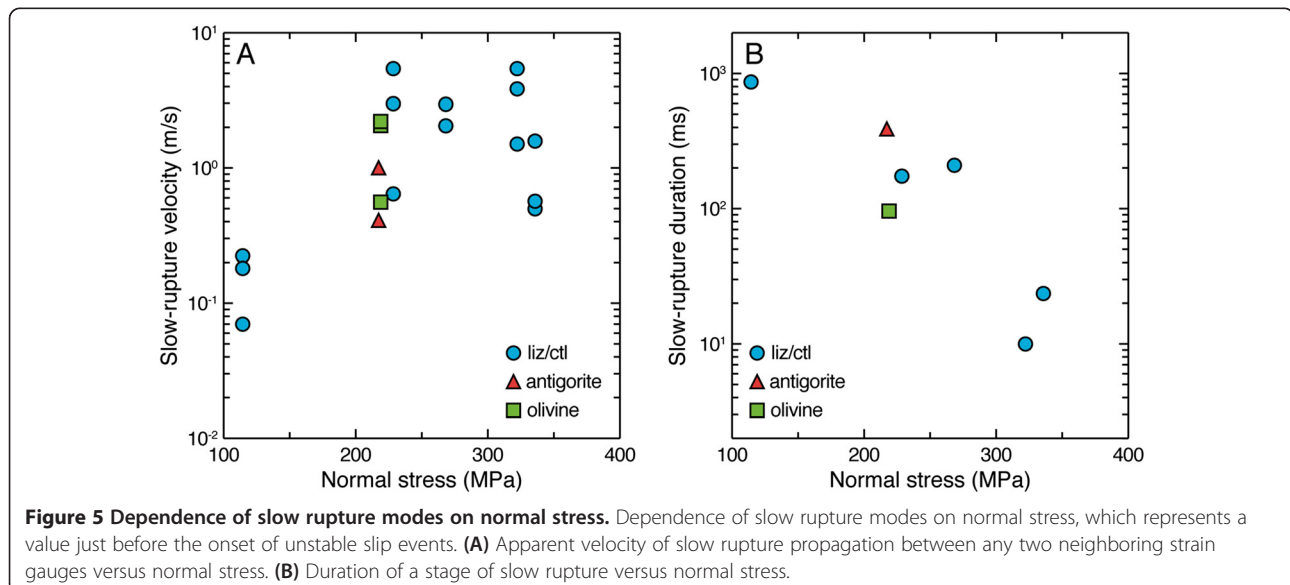
upwards at speeds in the range of 0.5 to 1.6 m/s. In the experiments conducted at $P_c = 60$ to 140 MPa for liz/ctl, the shear stress decreased very slowly toward a residual value over a protracted time period lasting approximately 1 s, with none of the aforementioned 'subsequent rapid drops' in shear stress or large oscillations (Figures 3C,F and 4). Furthermore, the measurements of local strain at $P_c = 60$ MPa show that a rupture seems to have nucleated at a location close to the lower edge of the saw-cut (orange gauge) just before the onset of the long approximately 1-s drop in shear stress (Figure 3F), and that it then propagated upward (toward the purple gauge) at speeds ranging from 0.07 to 0.22 m/s. Slow stick-slip behavior has been reported in recent friction experiments on lizardite-rich gouge conducted at room temperature (Kaproth and Marone 2013).

Note that the apparent velocities of fast rupture propagation determined in this study are not constrained to a high degree of accuracy, largely because of the relatively small-scale nature of the sample assembly. In some cases, the time difference between the arrival of a rupture front at two neighboring strain gauges could not be determined (e.g., the red and purple gauges in Figure 3D) because of the small size of the test sample and the limited sampling rate. However, they do provide reasonable first-order estimates of around 1.5 to 6.0 km/s based on the rough values calculated from our experimental data. For the three types of synthetic fault gouge studied, the apparent velocities of slow rupture propagation between all possible sets of any two neighboring strain gauges ranged from 0.07 to 5.43 m/s (Figure 5). The apparent rupture velocities seem to decrease with decreasing normal stress, at least from 268 to 114 MPa, but a large scatter is present in the data (Figure 5A). We estimated the slow rupture duration for each experiment based on the time interval during which the shear stress decreased at a slow rate. In addition, although the data are limited, the duration of a stage of slow rupture propagation appears to increase exponentially with decreasing normal stress (Figure 5B).

Microstructures

Polished thin sections were prepared from the experimentally deformed liz/ctl samples for petrographic analysis using an optical microscope. The jacketed samples were impregnated with epoxy resin before being sliced parallel to the shear direction and normal to the pre-cut surface. In the present paper, the labeling scheme for localized shears developed within gouge layers is adapted from Logan et al. (1992) (Figure 6).

Figure 5 Dependence of slow rupture modes on normal stress. Dependence of slow rupture modes on normal stress, which represents a value just before the onset of unstable slip events. **(A)** Apparent velocity of slow rupture propagation between any two neighboring strain gauges versus normal stress. **(B)** Duration of a stage of slow rupture versus normal stress.

The liz/ctl fault gouges deformed at 60, 100, 140, 160, and 170 MPa all contain narrow (10 to 50 μm), localized shear zones that occur directly adjacent to the gabbro cylinder on both sides of the gouge (referred to as B shears), which exhibit shear-zone-parallel planar fabrics defined by a preferred crystallographic orientation (Figure 7A-D). In detail, however, the liz/ctl fault gouge deformed at P_c = 60 MPa is also characterized by a series of regularly spaced, localized shear zones that are oriented oblique (approximately 10° to 15°) to the pre-cut surface (referred to as R_1 shears) (Figure 7A). Note that the total displacements before an unstable slip event takes place are smallest in the liz/ctl gouge deformed at P_c = 60 MPa. In contrast, the liz/ctl gouges deformed at P_c = 100 to 170 MPa contain a number of anastomosing shear zones that are oriented subparallel to the gouge-rock interface (referred to as Y shears) and that are separated by intervening lenticular regions in which the grains are found to be more massive, sub-equant, and less deformed overall (Figure 7C). The most well-developed Y shears often exhibit a wavy appearance and are in some cases associated with the formation of kink bands that are oriented parallel to the X- and R_2-shear directions (Figure 7B,D).

Discussion and conclusions
### Frictional behavior and microstructural evolution of fault gouges
All the liz/ctl gouges show grain size reduction by cataclasis, possibly resulting in strain hardening with the compaction and interlocking of the grains (e.g., Morrow et al. 1982). Previous laboratory experiments on gouge layers have shown that localization of deformation parallel to or along the gouge-rock interface (Y and B shears, respectively) with increasing displacement leads to rate-weakening friction or stick-slip instability (e.g., Logan et al. 1992; Beeler et al. 1996; Scruggs and Tullis 1998; Niemeijer et al. 2010; Ikari et al. 2011; Onuma et al. 2011). All liz/ctl gouges show the formation of obvious B shears, showing the strong preferred crystallographic orientation of serpentine, the width of which tends to increase with increasing confining pressure (i.e.,

Figure 6 Schematic diagram showing the relative orientations of various localized shear features. Schematic diagram showing the relative orientations of various localized shear features that may develop within a deformed fault gouge (after Logan et al., 1992).

compaction rate) and displacement, that is, an increase in shear strain. Furthermore, the R_1 shears that extend across the liz/ctl gouge layer in the lowest P_c experiments are not observed in the higher P_c experiments; alternatively, there are through-going Y shears in the gouge in the higher P_c experiments. These microstructural observations are in good agreement with those of Niemeijer et al. (2010), who found that increased shear strain leads to a reorientation of R_1 shears toward Y shears, resulting from the kinematic constraint of rigid forcing blocks on the gouge material (e.g., Mandl et al. 1977). We thus conclude that the fault gouges in this study evolved with strain from distributed deformation (cataclasis, grain rotation, and/or grain sliding) accompanied by faulting (through Riedel shears) in the strain-hardening range, to strain localization by the development of the B and Y shears in the strain-weakening range, which eventually leads to the unstable slip event.

Slow rupture process within gouge layers
Previous stick-slip experiments have been conducted on rocks to monitor the evolution of local shear stresses on bare surfaces (e.g., Johnson and Scholz 1976; Dieterich 1978; Okubo and Dieterich 1984; Ohnaka and Shen 1999). The individual stick-slip events occur in three distinct phases. In phase I, stable sliding begins to occur locally and then propagates laterally at a slow rate that is driven by the external loading. This local stable sliding corresponds to a slight decrease in the local shear stress. In phase II, the rupture propagates slowly and produces an instantaneous increase in the local shear stress in the vicinity of the propagating tip, clearly identifying the rupture front. The shear stress subsequently decreases considerably during the remainder of this phase. During phase III, unstable slip results in sharp stress drops and rapid rupture propagation at speeds comparable to the shear wave velocity of the sample. The similarity between phase I stable sliding and creep patch development was recently reported in the context of a numerical model (Bar-Sinai et al. 2013). Both stable sliding and creep patch development are influenced by the loading rate, but they are clearly differentiated from phase II slow rupture propagation.

Recent friction experiments on polymethyl-methacrylate (PMMA) have also shown that under various loading conditions, different modes of rupture may occur along the interface during a single stick-slip event (Rubinstein et al. 2004; Ben-David et al. 2010a, b; Nielsen et al. 2010). Rubinstein et al. (2004) observed a sharp transition from unstable, rapid sub-Rayleigh (limited by the Rayleigh wave speed) rupture to stable, slow (approximately 5% of V_s) rupture modes. Ben-David et al. (2010a) found that such rupture modes, ranging from slow (approximately 5% of V_s) to supershear velocity ($>V_s$), vary
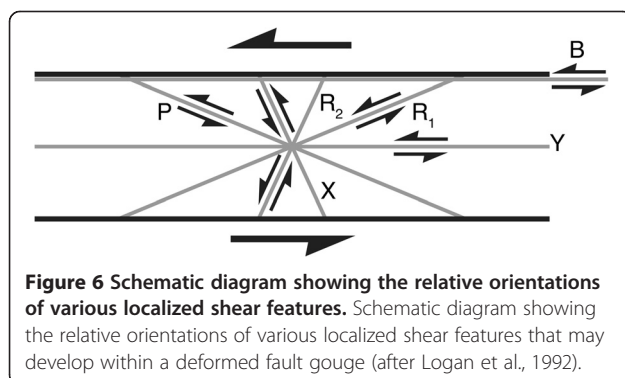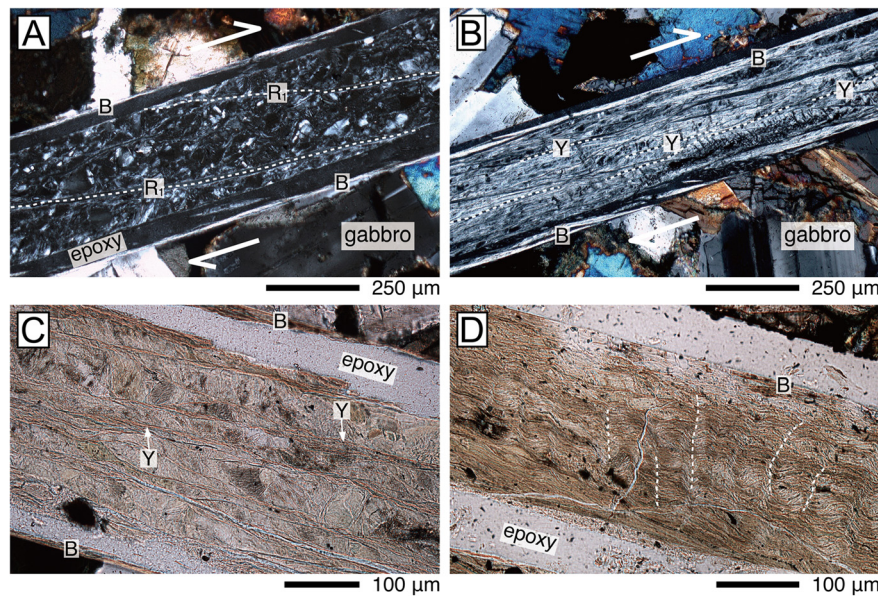
Figure 7 Optical photomicrographs of experimentally deformed liz/ctl, antigorite, and olivine synthetic fault gouges. Optical photomicrographs of experimentally deformed liz/ctl, antigorite, and olivine synthetic fault gouges observed in **(A and B)** cross-polarized light and **(C and D)** plane-polarized light. The shear sense along each fault gouge in **A** and **B** is indicated by the large white arrows. **(A)** Liz/ctl gouge ($P_c = 60$ MPa), highlighting the development of regularly spaced R_1 shears that curve in a listric fashion into the B shears present on either side of the gouge layer. **(B)** Liz/ctl gouge ($P_c = 140$ MPa), highlighting the development of a number of anastomosing Y and B shears, showing strong evidence of the preferred crystallographic orientation of serpentine (i.e., a distinctive shear-zone-parallel planar fabric). **(C)** Liz/ctl gouge ($P_c = 120$ MPa), highlighting well-developed, anastomosing Y and B shears that are interleaved with regions of intervening gouge where the mineral grains are more massive and less deformed. **(D)** Liz/ctl gouge ($P_c = 170$ MPa), highlighting the development of densely distributed Y shears that show a pronounced wavy appearance linked to the development of kink-bands oriented parallel to the X- and R_2-shear directions.

according to local differences in the ratio of shear stress to normal stress. In addition, Passelègue et al. (2013) performed stick-slip experiments on granite under a range of pressure conditions ($P_c = 10$ to 150 MPa), confirming that the transition between sub-Rayleigh and supershear ruptures depends on the ratio of initial shear stress to normal stress.

Here, our unstable slip experiments on synthetic gouge layers demonstrate a succession of different modes of rupture (Figure 4), consisting of a phase with nucleation/propagation events that take place at a slow velocity (approximately 0.1% of V_s), often followed by an unstable phase that eventually leads to the onset of high-speed rupture propagation (comparable in velocity to V_s). The shearing of simulated gouge layers in our experiments resulted in an unstable slip event that followed up to approximately 8 mm of stable sliding. During this stable sliding, we observed no instantaneous increases in the local shear stress (such as a clear bump to compression and subsequent extension) that would have indicated the propagation of a rupture tip. This indicates that the slow ruptures observed in this study (e.g., Figure 3) are neither the phase I events observed in previous rock-on-rock experiments nor creep patches reported in recent numerical modeling studies (Bar-Sinai et al., 2013).

We find that for the high-μ fault zone materials (i.e., antigorite and olivine), the slow rupture mode is too short to be detected by our experimental assembly (with strain gauges spaced at 3-mm intervals along the fault) at relatively high confining pressures (e.g., Figure 3A). In contrast, for the low-μ fault zone material (i.e., liz/ctl), we clearly observe consistent increases in the degree of development of the slow rupture mode with decreasing confining pressure; that is, a slow drop in shear stress predominates over a fast drop in shear stress with decreasing initial normal stress (e.g., compare the mean shear stress curve for liz/ctl in Figure 3B at 170 MPa with that in Figure 3C at 60 MPa). These observations suggest that sustained slow shear failure arises as a consequence of both low values of normal stress and low values of intrinsic gouge hardness (i.e., frictional strength).

Numerical simulations on the basis of rate- and state-dependent friction laws have succeeded in reproducing slow slip behavior with recurrence intervals similar to those of SSEs (e.g., Liu and Rice 2007, 2009; Rubin 2008). The simulations showed that the emergence of SSEs depends primarily on the parameter W/h^*, where W is the size of the unstable region and h^* is the nucleation size, and revealed that the propagation speed or duration of SSEs decreases or increases, respectively, with

decreasing W/h^*. From the theoretical estimate given by Rice (1993), h^* is inversely proportional to $\sigma_n (b - a)$, where σ_n is the effective normal stress, and a and b are the rate and state friction parameters, respectively, meaning that lower effective normal stress leads to a larger h^* (hence smaller W/h^*).

This finding is qualitatively consistent with our experiments in which the velocity and duration of slow rupture propagation events become lower and longer, respectively, with decreasing normal stress (at least from 268 to 114 MPa) (Figure 5). In addition, fault gouges with lower friction coefficients tend to have lower $(b - a)$ values, hence smaller W/h^* (e.g., Ikari et al. 2011). This scenario may help to explain why the slow rupture mode observed in this study is facilitated in the fault zone that exhibits lower friction. We also note that if the sample diameter used in our experiments were increased above 20 mm, the commensurate increase in the rate-and-state friction parameter, W, defined as the length of the fault surface (i.e., approximately 28 mm) in this study, would restrict slow rupture modes to conditions of lower normal stress.

Implications for slow slip events in subduction zones

It remains unclear whether all series of slow slip events, as seen in the laboratory (acrylic/analog and rock materials), nature (i.e., SSEs), and numerical simulations (based on rate and state friction), can be represented by a single friction law. Nevertheless, the apparent velocities of slow rupture propagation within the liz/ctl fault gouges, which range from 0.07 to 5.43 m/s at effective normal stresses of 114 to 268 MPa (Figure 5), are largely consistent with those documented for short-term SSEs in Japan and Cascadia (Table 1) (e.g., Hirose and Obara 2010; Gao et al. 2012). It is important to note that the hydration of the mantle wedge in subduction zones is expected to form antigorite rather than liz/ctl (e.g., Hirauchi et al. 2010b). Nevertheless, our observations lead us to conclude that long-term slip events (i.e., those with V_r much less than approximately 0.1 m/s) (e.g., Radiguet et al., 2011; Kobayashi, 2014) probably occur within a region of much lower effective normal stress, even if liz/ctl is assumed to be present along the slab-mantle interface. Indeed, models of rate-and-state friction assume an effective normal stress of only a few to several tens of MPa, in order to reproduce slow slip events with recurrence intervals consistent with those of SSEs (e.g., Liu and Rice 2007, 2009).

Our experiments were conducted under dry conditions, in order to eliminate the effect of pore fluids, such as fluid flow, thermal pressurization, and fluid-assisted chemical processes, on unstable slip behavior in this series of experiments (e.g., Moore and Lockner 2004;

Table 1 Slow-rupture velocity vs. shear wave velocity in different contexts

Context	V_r/V_s	Reference
Acrylic and resin (Laboratory)	4% to 8%	Rubinstein et al. (2004)
		Nielsen et al. (2010)
Serpentines (Laboratory)	0.003% to 0.23%	This study
Short-term SSEs (Nature)	0.002% to 0.007%	Ito et al. (2007)
		Hirose and Obara (2010)
		Schmidt and Gao (2010)
Long-term SSEs (Nature)	0.0003%	Radiguet et al. (2011)

Mitchell and Faulkner 2008; Brantut and Sulem 2012). Despite the dry conditions, we still observed slow slip events during our experiments on the low-μ fault zone material (i.e., liz/ctl) at low confining pressure (i.e., 60 to 140 MPa; Figure 3C). This suggests that variations in the duration and propagation velocity of SSEs (Gao et al. 2012) are primarily controlled by the balance between the effective normal stress conditions and the intrinsic properties of the fault zone material. However, we cannot exclude the possibility that other factors, such as dilatancy, neutral velocity dependence of $(a - b)$, and non-monotonic dependence of steady state friction on slip velocity, also contribute to the emergence of SSEs in subduction zones (e.g., Liu and Rice 2009; Rubin 2008; Liu and Rubin 2010; Hawthorne and Rubin 2013).

Author details
[1]Department of Geosciences, Graduate School of Science, Shizuoka University, 836 Ohya, Suruga-ku, Shizuoka 422-8529, Japan. [2]Department of Earth Science, Graduate School of Science, Tohoku University, 6-3 Aramaki-Aza-Aoba, AobaSendai, Miyagi 980-8578, Japan.

References

Audet P, Bostock MG, Christensen NI, Peacock SM (2009) Seismic evidence for overpressured subducted oceanic crust and megathrust fault sealing. Nature 457:76–78

Bar Sinai Y, Brener EA, Bouchbinder E (2012) Slow rupture of frictional interfaces. Geophys Res Lett 39, L03308

Bar-Sinai Y, Spatschek R, Brener EA, Bouchbinder E (2013) Instabilities at frictional interfaces: creep patches, nucleation, and rupture fronts. Phys Rev E 88:060403(R)

Beeler NM, Tullis TE, Blanpied ML, Weeks JD (1996) Frictional behavior of large displacement experimental faults. J Geophys Res 101:8697–8715

Ben-David O, Cohen G, Fineberg J (2010a) The dynamics of the onset of frictional slip. Science 330:211–214

Ben-David O, Rubinstein SM, Fineberg J (2010b) Slip-stick and the evolution of frictional strength. Nature 463:76–79

Beroza GC, Ide S (2011) Slow earthquakes and nonvolcanic tremor. Annu Rev Earth Planet Sci 39:271–296

Brantut N, Sulem J (2012) Strain localization and slip instability in a strain-rate hardening, chemically weakening material. J Appl Mech 79:031004

Dengo CA, Logan JM (1981) Implications of the mechanical and frictional behavior of serpentinite to seismogenic faulting. J Geophys Res 86:10771–10782

Dieterich JH (1978) Preseismic fault slip and earthquake prediction. J Geophys Res 83:3940–3948

Dragert H, Wang K, James TS (2001) A silent slip event on the deeper Cascadia subduction interface. Science 292:1525–1528

Gao H, Schmidt DA, Weldon RJ II (2012) Scaling relationships of source parameters for slow slip events. Bull Seismol Soc Am 102:352–360

Hawthorne JC, Rubin AM (2013) Short-time scale correlation between slow slip and tremor in Cascadia. J Geophys Res 118:1316–1329

Hirauchi K, den Hartog SAM, Spiers CJ (2013) Weakening of the slab-mantle wedge interface induced by metasomatic growth of talc. Geology 41:75–78

Hirauchi K, Katayama I (2013) Rheological contrast between serpentine species and implications for slab-mantle wedge decoupling. Tectonophysics 608:545–551

Hirauchi K, Katayama I, Uehara S, Miyahara M, Takai Y (2010a) Inhibition of subduction thrust earthquakes by low-temperature plastic flow in serpentine. Earth Planet Sci Lett 295:349–357

Hirauchi K, Michibayashi K, Ueda H, Katayama I (2010b) Spatial variations in antigorite fabric across a serpentinite subduction channel: insights from the Ohmachi Seamount, Izu-Bonin frontal arc. Earth Planet Sci Lett 299:196–206

Hirose H, Obara K (2010) Recurrence behavior of short-term slow slip and correlated nonvolcanic tremor episodes in western Shikoku, southwest Japan. J Geophys Res 115:B00A21

Ikari MJ, Marone C, Saffer DM (2011) On the relation between fault strength and frictional stability. Geology 39:8386

Ide S, Beroza GC, Shelly DR, Uchide T (2007) A scaling law for slow earthquakes. Nature 447:76–79

Ito Y, Obara K, Shiomi K, Sekine S, Hirose H (2007) Slow earthquakes coincident with episodic tremors and slow slip events. Science 315:503–506

Johnson TL, Scholz CH (1976) Dynamic properties of stick-slip friction of rock. J Geophys Res 81:881–888

Kaneko Y, Ampuero J-P (2011) A mechanism for preseismic steady rupture fronts observed in laboratory experiments. Geophys Res Lett 38, L21307

Kaproth BM, Marone C (2013) Slow earthquakes, preseismic velocity changes, and the origin of slow frictional stick-slip. Science 341:1229–1232

Kato A, Iidaka T, Ikuta R, Yoshida Y, Katsumata K, Iwasaki T et al (2010) Variations of fluid pressure within the subducting oceanic crust and slow earthquakes. Geophys Res Lett 37, L14310

Kato N, Yamamoto K, Yamamoto H, Hirasawa T (1992) Strain-rate effect on frictional strength and the slip nucleation process. Tectonophysics 211:269–282

Kawano S, Katayama I, Okazaki K (2011) Permeability anisotropy of serpentinite and fluid pathways in a subduction zone. Geology 39:939–942

Kobayashi A (2014) A long-term slow slip event from 1996 to 1997 in the Kii Channel, Japan. Earth Planets Space 66:9

Liu Y, Rice JR (2007) Spontaneous and triggered aseismic deformation transients in a subduction fault model. J Geophys Res 112, B09404

Liu Y, Rice JR (2009) Slow slip predictions based on granite and gabbro friction data compared to GPS measurements in northern Cascadia. J Geophys Res 114, B09407

Liu Y, Rubin AM (2010) Role of fault gouge dilatancy on aseismic deformation transients. J Geophys Res 115, B10414

Logan JM, Dengo CA, Higgs NG, Wang ZZ (1992) Fabrics of experimental fault zones: their development and relationship to mechanical behavior. In: Evans B, Wong T-F (eds) Fault mechanics and transport properties of rock. Academic, London, pp 33–67

Mandl G, de Jong LNJ, Maltha A (1977) Shear zones in granular material. Rock Mech 9:95–144

Mitchell TM, Faulkner DR (2008) Experimental measurements of permeability evolution during triaxial compression of initially intact crystalline rocks and implications for fluid flow in fault zones. J Geophys Res 113, B11412

Moore DE, Lockner DA (2004) Crystallographic controls on the frictional behavior of dry and water-saturated sheet structure minerals. J Geophys Res 109, B03401

Moore DE, Lockner DA, Tanaka H, Iwata K (2004) The coefficient of friction of Chrysotile gouge at seismogenic depth. Int Geol Rev 46:385–398

Morrow CA, Shi LQ, Byerlee JD (1982) Strain hardening and strength of clay-rich fault gouges. J Geophys Res 87:6771–6780

Nielsen S, Taddeucci J, Vinciguerra S (2010) Experimental observation of stick-slip instability fronts. Geophys J Int 180:697–702

Niemeijer A, Marone C, Elsworth D (2010) Frictional strength and strain weakening in simulated fault gouge: competition between geometrical weakening and chemical strengthening. J Geophys Res 115, B10207

Obara K (2002) Nonvolcanic deep tremor associated with subduction in southwest Japan. Science 296:1679–1681

Ohnaka M, Shen L (1999) Scaling of the shear rupture process from nucleation to dynamic propagation: implications of geometric irregularity of the rupturing surfaces. J Geophys Res 104:817–844

Okubo PG, Dieterich JH (1984) Effects of physical fault properties on frictional instabilities produced on simulated faults. J Geophys Res 89:5817–5827

Onuma K, Muto J, Nagahama H, Otsuki K (2011) Electric potential changes associated with nucleation of stick–slip of simulated gouges. Tectonophysics 502:308–314

Passelègue FX, Schubnel A, Nielsen S, Bhat HS, Madariaga R (2013) From sub-rayleigh to supershear ruptures during stick-slip experiments on crustal rocks. Science 340:1208–1211

Peacock SM, Christensen NI, Bostock MG, Audet P (2011) High pore pressures and porosity at 35 km depth in the Cascadia subduction zone. Geology 39:471–474

Peng Z, Gomberg J (2010) An integrated perspective of the continuum between earthquakes and slow-slip phenomena. Nat Geosci 3:599–607

Radiguet M, Cotton F, Vergnolle M, Campillo M, Valette B, Kostoglodov V, Cotte N (2011) Spatial and temporal evolution of a long term slow slip event: the 2006 Guerrero Slow Slip Event. Geophysical Journal International 184:816–828

Reinen LA, Weeks JD, Tullis TE (1994) The frictional behavior of lizardite and antigorite serpentinites: experiments, constitutive models, and implications for natural faults. Pure Appl Geophys 143:317–358

Rice JR (1993) Spatio-temporal complexity of slip on a fault. J Geophys Res 98:9885–9907

Rogers G, Dragert H (2003) Episodic tremor and slip on the Cascadia subduction zone: the chatter of silent slip. Science 300:1942–1943

Rubin AM (2008) Episodic slow slip events and rate-and-state friction. J Geophys Res 113, B11414

Rubinstein SM, Cohen G, Fineberg J (2004) Detachment fronts and the onset of dynamic friction. Nature 430:1005–1009

Schmidt DA, Gao H (2010) Source parameters and time-dependent slip distributions of slow slip events on the Cascadia subduction zone from 1998 to 2008. Journal of Geophysical Research 115:B00A18

Scruggs VJ, Tullis TE (1998) Correlation between velocity dependence of friction and strain localization in large displacement experiments on feldspar, muscovite and biotite gouge. Tectonophysics 295:15–40

Shelly DR, Beroza GC, Ide S, Nakamula S (2006) Low-frequency earthquakes in Shikoku, Japan, and their relationship to episodic tremor and slip. Nature 442:188–191

Wicks FJ, Whittaker EJW (1977) Serpentine textures and serpentinization. Can Mineral 15:459–488